Holographic nature of three-wave mixing

Maria Bondani* and Alessandra Andreoni

Dipartimento di Scienze Chimiche, Fisiche e Matematiche, Universitá degli Studi dell'Insubria and Istituto Nazionale di Fisica della Materia, INFM, Unitá di Como, via Valleggio, 11, 22100 Como, Italy

(Received 17 January 2002; revised manuscript received 17 May 2002; published 16 September 2002)

Three-wave interactions occurring in conditions of type I phase matching in a uniaxial crystal are considered in the general case of noncollinear wave propagation. It is demonstrated that, if one among the interacting fields at ω_i $(i=1,2,3)$ is virtually unaffected in amplitude by the interaction, the remaining two fields at ω_j $(j\neq i)$ are holographic replicas of each other, the constant field acting as the reference field in holography. Experiments are presented in which a holographic image of an object consisting in a pointlike light source is obtained by either up- or down-conversion for any choice of the object- and reference-field frequencies among ω_1, ω_2, and ω_3.

DOI: 10.1103/PhysRevA.66.033805 PACS number(s): 42.65.Ky, 42.65.Hw, 42.40.−i, 42.30.−d

INTRODUCTION

Nowadays, the fast response achieved by real-time holographic techniques and the high space resolution inherent to holography are extensively used in different scientific and technical fields such as information processing and optical computing [1–4]. Some of these techniques adopt third-order nonlinear media endowed with particularly fast response as the recording materials. Recently, we demonstrated the generation of real-time holograms through a second-order nonlinear interaction, namely, noncollinear second-harmonic generation [5–8]. In our case the recording and reconstruction stages occur simultaneously and the time response can be as short as tens of femtoseconds [9,10]. As far as we know, before our work $\chi^{(2)}$ effects were never used to obtain holographic wave-front transformations and only seldom for wave-front transformations performed for other purposes; namely, to enhance the detectability of a weak coherent image-bearing signal embedded in random noise [11–13], to improve the beam quality of laser sources [14–20], and to generate spatial solitons [21]. In this paper we show that within the parametric approximation any three-wave interaction occurring in type I phase matching (PM I) among waves that propagate noncollinearly to each other instantaneously produces a holographic image of the incident object field. The object field at the entrance of the nonlinear crystal is thought of in terms of its plane-wave expansion, which allows a rather straightforward description of the nonlinear interaction. We substantiate our theory with experiments in which the object field emitted by a pointlike source is any of the three interacting fields (that is, at any of the frequencies ω_1, ω_2, ω_3, with $\omega_3=\omega_2+\omega_1$) and the holographic field is generated at either the sum or the difference frequency.

I. THEORY

We consider the interaction among three amplitude-modulated plane waves, $\boldsymbol{E}_1(\boldsymbol{r},t)$ and $\boldsymbol{E}_2(\boldsymbol{r},t)$ with ordinary polarization and $\boldsymbol{E}_3(\boldsymbol{r},t)$ with extraordinary polarization, in a $\chi^{(2)}$ nonlinear uniaxial crystal. As depicted in Fig. 1 the waves propagate in the (y,z) plane at different angles ϑ_1, ϑ_2 and ϑ_3 to the direction z, which is perpendicular to the crystal entrance face. Note that the extraordinarily polarized field $\boldsymbol{E}_3$ is not transverse. With reference to the figure, we can write the fields interacting at position $\boldsymbol{r}\equiv(x,y,z)$ in any plane at fixed x as follows:

$$\boldsymbol{E}_1(\boldsymbol{r},t)=\frac{\hat{\boldsymbol{x}}}{2}\left\{\sqrt{\frac{2\eta_0\hbar\omega_1}{n_1}}a_1(\boldsymbol{r})\times\exp[-i(k_1\cos\vartheta_1 z+k_1\sin\vartheta_1 y-\omega_1 t)]+\text{c.c.}\right\},$$

$$\boldsymbol{E}_2(\boldsymbol{r},t)=\frac{\hat{\boldsymbol{x}}}{2}\left\{\sqrt{\frac{2\eta_0\hbar\omega_2}{n_2}}a_2(\boldsymbol{r})\times\exp[-i(k_2\cos\vartheta_2 z+k_2\sin\vartheta_2 y-\omega_2 t)]+\text{c.c.}\right\},$$

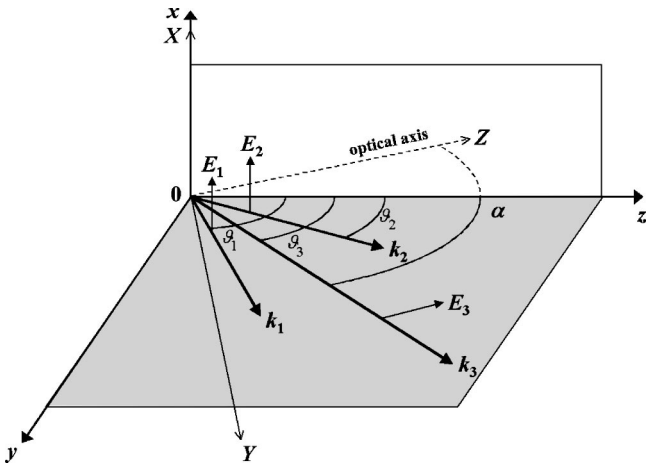

FIG. 1. Noncollinear three-wave interaction in a type I uniaxial crystal. (X,Y,Z): crystal reference frame with Z parallel to the optical axis; (x,y,z): laboratory reference frame with the (x,y) plane coinciding with the crystal entrance face; α: tuning angle.

*Electronic address: maria.bondani@uninsubria.it

$$\boldsymbol{E}_3(\boldsymbol{r},t)=\frac{1}{2}\left\{\sqrt{\frac{2\eta_0\hbar\omega_3}{n_3}}[\hat{\boldsymbol{y}}a_{3y}(\boldsymbol{r})+\hat{\boldsymbol{z}}a_{3z}(\boldsymbol{r})]\right.$$
$$\left.\times\exp[-i(k_3\cos\vartheta_3 z+k_3\sin\vartheta_3 y-\omega_3 t)]+\text{c.c.}\right\}, \tag{1}$$

in which η_0 is the vacuum impedance, and $a_j(\boldsymbol{r})=|a_j(\boldsymbol{r})|\exp[i\Lambda_j(\boldsymbol{r})]$ are the complex envelopes of the interacting fields with wave vectors $k_j=n_j\omega_j/c$ and frequencies ω_1, ω_2, and ω_3 (n_j are the corresponding indices of refraction). For frequencies satisfying energy conservation ($\omega_3=\omega_2+\omega_1$), the classical Maxwell equations describing the noncollinear interaction in the geometry depicted in Fig. 1 yield the set of equations (see the Appendix)

$$\sin\vartheta_1\frac{\partial a_1(\boldsymbol{r})}{\partial y}+\cos\vartheta_1\frac{\partial a_1(\boldsymbol{r})}{\partial z}$$
$$=i[g_+a_{3y}(\boldsymbol{r})+g_-a_{3z}(\boldsymbol{r})]a_2^*(\boldsymbol{r})$$
$$\times\exp[-i(\Delta k_\parallel z+\Delta k_\perp y)],$$

$$\sin\vartheta_2\frac{\partial a_2(\boldsymbol{r})}{\partial y}+\cos\vartheta_2\frac{\partial a_2(\boldsymbol{r})}{\partial z}$$
$$=i[g_+a_{3y}(\boldsymbol{r})+g_-a_{3z}(\boldsymbol{r})]a_1^*(\boldsymbol{r})$$
$$\times\exp[-i(\Delta k_\parallel z+\Delta k_\perp y)],$$

$$\sin\vartheta_3\frac{\partial a_{3y}(\boldsymbol{r})}{\partial y}+\cos\vartheta_3\frac{\partial a_{3y}(\boldsymbol{r})}{\partial z}$$
$$=ig_+a_1(\boldsymbol{r})a_2(\boldsymbol{r})\exp[i(\Delta k_\parallel z+\Delta k_\perp y)],$$

$$\sin\vartheta_3\frac{\partial a_{3z}(\boldsymbol{r})}{\partial y}+\cos\vartheta_3\frac{\partial a_{3z}(\boldsymbol{r})}{\partial z}$$
$$=ig_-a_1(\boldsymbol{r})a_2(\boldsymbol{r})\exp[i(\Delta k_\parallel z+\Delta k_\perp y)], \tag{2}$$

where the (real) coupling constants g_+ and g_- are

$$g_{+,-}=d_{+,-}\sqrt{\frac{2\hbar\omega_1\omega_2\omega_3\eta_0^3}{n_1n_2n_3}}. \tag{3}$$

The coupling constants $d_{+,-}$ are defined in the Appendix, and

$$\Delta k_\parallel=k_3\cos\vartheta_3-k_1\cos\vartheta_1-k_2\cos\vartheta_2,$$
$$\Delta k_\perp=k_3\sin\vartheta_3-k_1\sin\vartheta_1-k_2\sin\vartheta_2, \tag{4}$$

are the phase mismatch components along the z and y directions.

In analogy with holography, we take only two nonvanishing fields entering the crystal at $z=0$, one of which, according to the parametric approximation, is assumed to propagate with constant envelope during the interaction (reference field) and the other is emitted/diffused by the object. Moreover, the solutions of interest, which we use to interpret our experimental results, are those for negligible phase mismatch. The structure of the coupled equations in system (2) is such that three different choices of boundary conditions at $z=0$ are relevant. Note that the fields at the crystal entrance are always assumed to be transverse and, in the case of a nonvanishing $\boldsymbol{E}_3$ field entering the crystal (see Fig. 1); this assumption implies

$$-\frac{a_{3y}(0)}{\cos\vartheta_3}=\frac{a_{3z}(0)}{\sin\vartheta_3}\equiv a_3(0). \tag{5}$$

By using Eqs. (A8) and (3), Eq. (5) yields

$$g_+a_{3y}(0)+g_-a_{3z}(0)$$
$$=(d_{22}\cos\alpha+d_{31}\sin\alpha)\sqrt{\frac{2\hbar\omega_1\omega_2\omega_3\eta_0^3}{n_1n_2n_3}}a_3(0)$$
$$\equiv g_{eff}a_3(0), \tag{6}$$

which will be useful later [see Eq. (17)]. The three sets of interesting boundary conditions are as follows.

(1) Sum-frequency generation

$$a_1(0)\neq 0,\ a_2(z)=a_2(0),\ \text{and}\ a_3(0)=0, \tag{7}$$

where field 1 is taken as the object field, field 2 as the reference field (with constant envelope), and field 3 a generated field.

(2) Difference-frequency generation (DFG, object field at high frequency ω_3)

$$a_1(0)=0,\ a_2(z)=a_2(0),\ \text{and}\ a_3(0)\neq 0 \tag{8}$$

with field 3 as the object field, field 2 as the reference field, and field 1 as the generated field.

(3) Difference-frequency generation (DFG, object field at low frequency ω_1)

$$a_1(0)\neq 0,\ a_2(0)=0,\ \text{and}\ a_3(z)=a_3(0) \tag{9}$$

with field 1 as the object field, field 3 as the reference field, and field 2 as the generated field. The three cases will be discussed separately, for $\Delta k_\parallel=\Delta k_\perp=0$, since the generated fields produce different kinds of holographic images.

(1) The general solution to system (2) for the amplitude of the holographic field generated at the sum frequency is

$$a_{3y,3z}(y,z)=\frac{g_{+,-}}{g}a_1(0)\sin\left\{\frac{g|a_2(0)|}{\sin(\vartheta_1-\vartheta_3)}\right.$$
$$\left.\times[(\cos\vartheta_3-\cos\vartheta_1)y-(\sin\vartheta_3-\sin\vartheta_1)z]\right\}$$
$$\times\exp\left\{i\left[\Lambda_2(0)+\frac{\pi}{2}\right]\right\}, \tag{10}$$

where

$$g=\sqrt{g_+^2+g_-^2}. \tag{11}$$

According to the definitions in Eq. (1), the holographic field can be written as

$$\boldsymbol{E}_3(y,z,t)=\sqrt{\frac{2\eta_0\hbar\omega_3}{n_3}}\frac{\hat{\boldsymbol{y}}g_+ +\hat{\boldsymbol{z}}g_-}{2g}\times a_1(0)\sin\left[\frac{g|a_2(0)|}{\cos[(\vartheta_3-\vartheta_1)/2]}\left(\sin\frac{\vartheta_3+\vartheta_1}{2}y+\cos\frac{\vartheta_3+\vartheta_1}{2}z\right)\right]\exp\left\{i\left[\Lambda_2(0)+\frac{\pi}{2}\right]\right\}\times\exp[-i(k_3\cos\vartheta_3 z+k_3\sin\vartheta_3 y-\omega_3 t)]+\text{c.c.} \tag{12}$$

and by defining the unit vector $\hat{\boldsymbol{w}}$ in the direction of $(\hat{\boldsymbol{y}}g_+ +\hat{\boldsymbol{z}}\,g_-)$, as

$$\boldsymbol{E}_3(y,z,t)=\frac{\hat{\boldsymbol{w}}}{2}\sqrt{\frac{2\eta_0\hbar\omega_3}{n_3}}\{a_3(y,z)\times\exp[-i(k_3\cos\vartheta_3 z+k_3\sin\vartheta_3 y-\omega_3 t)]+\text{c.c.}\} \tag{13}$$

in which

$$a_3(y,z)=a_1(0)\sin\left[\frac{g|a_2(0)|}{\cos[(\vartheta_3-\vartheta_1)/2]}\times\left(\sin\frac{\vartheta_3+\vartheta_1}{2}y+\cos\frac{\vartheta_3+\vartheta_1}{2}z\right)\right]\times\exp\left\{i\left[\Lambda_2(0)+\frac{\pi}{2}\right]\right\}. \tag{14}$$

From the expression in Eq. (14), we see that the amplitude of the holographic field $a_3(y,z)$ at any position inside the crystal is directly proportional to the amplitude of the object field $a_1(0)$ at the entrance of the crystal through a complex function of the position along the z axis (see Fig. 1). That is, the field $\boldsymbol{E}_3(z,t)$ generated at the sum frequency indeed reconstructs a holographic image [5,6,22,23]. Moreover, since the proportionality in Eq. (14) is direct, the holographic image of a real object is virtual, and vice versa [23]. The virtual nature of the holographic image of a real object implies the disadvantage that at least a lens is necessary to make the holographic image detectable and usable, for instance, inside a full-optical logic circuit [5–8,24].

(2) In this case of DFG, the solution to system (2) for the holographic field amplitude is

$$a_1(y,z)=\frac{g_{eff}}{g}a_3(0)\sin\left\{\frac{g|a_2(0)|}{\sin(\vartheta_1-\vartheta_3)}[(\cos\vartheta_3-\cos\vartheta_1)y-(\sin\vartheta_3-\sin\vartheta_1)z]\right\}\exp\left\{i\left[-\Lambda_2(0)+\frac{\pi}{2}\right]\right\} \tag{15}$$

and hence

$$\boldsymbol{E}_1(y,z,t)=\frac{\hat{x}}{2}\sqrt{\frac{2\eta_0\hbar\omega_1}{n_1}}a_3(0)\sin\left[\frac{g|a_2(0)|}{\cos[(\vartheta_3-\vartheta_1)/2]}\times\left(\sin\frac{\vartheta_3+\vartheta_1}{2}y+\cos\frac{\vartheta_3+\vartheta_1}{2}z\right)\right]\times\exp\left\{i\left[-\Lambda_2(0)+\frac{\pi}{2}\right]\right\}\exp[-i(k_1\cos\vartheta_1 z+k_1\sin\vartheta_1 y-\omega_1 t)]+\text{c.c.} \tag{16}$$

As in the previous case, the holographic field amplitude in Eq. (15) is directly proportional to the amplitude of the object field at the entrance of the crystal. Thus, this kind of DFG also produces a virtual holographic image of a real object, and vice versa. By applying case 1 and case 2 in cascade one could then realize an all-optical circuit. In fact, if we start with an input (object field) at a given frequency (say ω_1) and perform a sum-frequency generation with a reference field at ω_2, we get a virtual holographic image at ω_3 as the output. If we now down-convert the virtual image at ω_3 by using the same reference field at ω_2 , we get a real holographic image of the initial object, again at ω_1, which eventually can be reused as the input of another all-optical circuit. Since the object entering this down-conversion step is actually a virtual image at ω_3 carried by a nontransverse field [field $\boldsymbol{E}_3$ in Eq. (13)], the output of this step would still be represented by Eq. (16) but without the substitution defined in Eq. (6).

(3) In the other case of DFG, the expression for the holographic field amplitude is

$$a_2(y,z)=a_1^*(0)\sinh\left\{\frac{g_{eff}|a_3(0)|}{\sin(\vartheta_1-\vartheta_2)}[(\cos\vartheta_2-\cos\vartheta_1)y-(\sin\vartheta_2-\sin\vartheta_1)z]\right\}\exp\left\{i\left[\Lambda_3(0)+\frac{\pi}{2}\right]\right\} \tag{17}$$

from which

$$\boldsymbol{E}_2(y,z,t)=\frac{\hat{x}}{2}\sqrt{\frac{2\eta_0\hbar\omega_2}{n_2}}a_1^*(0)\sinh\left[\frac{g_{eff}|a_3(0)|}{\cos[(\vartheta_1-\vartheta_1)/2]}\times\left(\sin\frac{\vartheta_1+\vartheta_2}{2}y+\cos\frac{\vartheta_1+\vartheta_2}{2}z\right)\right]\times\exp\left\{i\left[\Lambda_3(0)+\frac{\pi}{2}\right]\right\}\exp[-i(k_2\cos\vartheta_2 z+k_2\sin\vartheta_2 y-\omega_2 t)]+\text{c.c.} \tag{18}$$

At variance with the previous situations, Eq. (17) shows that the holographic field amplitude $a_2(y,z)$ is proportional to the phase-conjugated complex amplitude $a_1^*(0)$ of the object field. Thus, this DFG produces a holographic field that reconstructs an image of the same nature as that of the object (real from real and virtual from virtual) [23]. This has the obvious advantage of making it straightforward to detect the holographic image of a real object. Moreover, in the degenerate case $\omega_2=\omega_1=\omega_3/2$, the real holographic image can be

reused in an all-optical circuit. Finally, we note that the analytical solution in Eq. (18) constitutes a substantial generalization of the results obtained by numerical integration of the coupled nonlinear equations in [19] for degenerate parametric amplification in collinear propagation geometry.

We analyze the space-dependent phases of the fields obtained above to determine how the wave front of the object field transforms into the wave front of the corresponding holographic field in each of the cases examined. By defining the space-dependent phases $\varphi_j(\boldsymbol{r})$ of the fields $\boldsymbol{E}_j(\boldsymbol{r},t)$ so that $\boldsymbol{E}_j(\boldsymbol{r},t)=\boldsymbol{E}_j(\boldsymbol{r},0)\exp\{i[\varphi_j(\boldsymbol{r})+\omega_j t]\}$, in phase matching ($\boldsymbol{k}_3=\boldsymbol{k}_1+\boldsymbol{k}_2$) for the holographic field in Eq. (13) generated at the sum frequency with the help of Eq. (14) we find for

case 1,

$$\varphi_3(\boldsymbol{r})=\Lambda_1(0)+\Lambda_2(0)+\frac{\pi}{2}-\boldsymbol{k}_3\cdot\boldsymbol{r}, \tag{19}$$

and for the two fields obtained by DFG in Eq. (16) and in Eq. (18)

case 2,

$$\varphi_1(\boldsymbol{r})=-\Lambda_2(0)+\Lambda_3(0)+\frac{\pi}{2}-\boldsymbol{k}_1\cdot\boldsymbol{r}, \tag{20}$$

case 3,

$$\varphi_2(\boldsymbol{r})=-\Lambda_1(0)+\Lambda_3(0)+\frac{\pi}{2}-\boldsymbol{k}_2\cdot\boldsymbol{r}. \tag{21}$$

Apart from the constant phase shift $\pi/2$, Eqs. (19)–(21) can be rewritten as

$$\varphi_3(\boldsymbol{r})=\varphi_1(\boldsymbol{r})+\varphi_2(\boldsymbol{r}), \tag{19$'$}$$

$$\varphi_1(\boldsymbol{r})=\varphi_3(\boldsymbol{r})-\varphi_2(\boldsymbol{r}), \tag{20$'$}$$

$$\varphi_2(\boldsymbol{r})=\varphi_3(\boldsymbol{r})-\varphi_1(\boldsymbol{r}). \tag{21$'$}$$

From now on we will discuss the degenerate case $\omega_1=\omega_2$ $(=\omega)$ which, due to type I phase matching, implies $k_1=k_2$. It is convenient to define the eikonals $L_j(\boldsymbol{r})$ so that $\varphi_j(\boldsymbol{r})=-k_jL_j(\boldsymbol{r})$. For our plane waves we have $L_j(\boldsymbol{r})=\hat{\boldsymbol{k}}_j\cdot\boldsymbol{r}$ being $\hat{\boldsymbol{k}}_j$ unit vectors parallel to the wave vectors and we can rewrite Eqs. (22–24) as follows:

case 1,

$$L_3(\boldsymbol{r})=\frac{L_1(\boldsymbol{r})+L_2(\boldsymbol{r})}{2\cos[(\vartheta_2-\vartheta_1)/2]}, \tag{22}$$

case 2,

$$L_1(\boldsymbol{r})=2\cos(\vartheta_3-\vartheta_2)L_3(\boldsymbol{r})-L_2(\boldsymbol{r}), \tag{23}$$

case 3,

$$L_2(\boldsymbol{r})=2\cos(\vartheta_3-\vartheta_1)L_3(\boldsymbol{r})-L_1(\boldsymbol{r}). \tag{24}$$

Equations (22)–(24) can be used in the case of non-plane-wave fronts by taking the unit vectors $\hat{\boldsymbol{k}}_j$ at each point $\boldsymbol{r}$ on the wave front parallel to the propagation direction at that point and $\vartheta_j=\vartheta_j(\boldsymbol{r})$. We assume as known the constant-phase surfaces (wave fronts) of the two fields in the right-hand sides of each of these equations and use them to determine the shape of the wave front of the third field(s). We consider object fields with spherical wave fronts and reference fields represented by plane waves and discuss the implications of Eqs. (22)–(24) as to the shapes of the generated wave fronts in cases 1, 2, and 3 separately. Note that, for a spherical object wave front of radius R, the eikonal with respect to an origin taken at the wave-front center is $L=R$ and that, for a plane reference wave front, L is simply its distance from the origin. With reference to panel (1) of Fig. 2, in case 1 the object and reference wave fronts, W_1 and W_2, respectively, with $L_1=R$ and $L_2=OH$ crossing at P generate a second-harmonic field with wave vector $\boldsymbol{k}_3$ along the bisector of the angle $P\hat{O}H=\vartheta_2-\vartheta_1(P)$ and eikonal $L_3(P)$ given by Eq. (22). Since $L_3(P)\cos\{[\vartheta_2-\vartheta_1(P)]/2\}$ represents the distance of the midpoint M of segment HC from the origin O, Eq. (22) allows one to find the wave front W_3 of the second-harmonic generated (SHG) holographic field via a simple geometrical construction at other directions also.

This is shown on the left-hand side of panel (1) in Fig. 2. To find the position Q of W_3 along the direction of $\hat{\boldsymbol{k}}_1$, the bisector of the angle between $\hat{\boldsymbol{k}}_1$ and $\hat{\boldsymbol{k}}_2$ must be drawn and intercepted by the perpendicular to $\hat{\boldsymbol{k}}_2$ from M. From this intercept the perpendicular to the bisector is drawn and Q is located where it crosses the straight line with direction $\hat{\boldsymbol{k}}_1$. If the actual object wave front transformed into W_3 is only a small region of the spherical wave front W_1, W_3 is virtually spherical with radius $2R$ since all $\hat{\boldsymbol{k}}_3$ unit vectors, not only the one at point P, cross each other at point O, where $OO'=OC=R$. Therefore the hologram of a point source generated at 2ω according to case 1 produces a pointlike image at a distance which is twice that of the object from the crystal $BaBO_3$ (BBO). The SHG hologram of an extended object would be not only located at double distance but also enlarged by a factor of 2 along the average propagation direction of the wave front W_3, while the transverse dimensions of object and holographic replica would obviously be the same [6].

The situation in case 2 is depicted in Fig. 2, panel (2). Here $L_3=R$ and $L_2=OH$ and the object and reference wave fronts crossing at point P are W_3 and W_2, respectively. Equation (23) which allows one to find the wave front W_1 of the field generated by DFG is identical to Eq. (22) once it is taken into account that $\vartheta_3=(\vartheta_2+\vartheta_1)/2$. Thus point N on W_3 is the midpoint of segment HD and, within the same approximation as above, the wave front W_1 is spherical and centered at point O', where $OO'=R/2$. This DFG holographic image is then nearer to the crystal BBO and longitudinally compressed by a factor of 2 compared to the object.

In case 3, $L_1=R$ and $L_3=OH$ as shown in Fig. 2, panel (3). Since Eq. (24) can be written as

$$\frac{L_2(\boldsymbol{r})}{\cos(\vartheta_2-\vartheta_3)}-L_3(\boldsymbol{r})=-\left[\frac{L_1(\boldsymbol{r})}{\cos(\vartheta_3-\vartheta_1)}-L_3(\boldsymbol{r})\right] \tag{25}$$

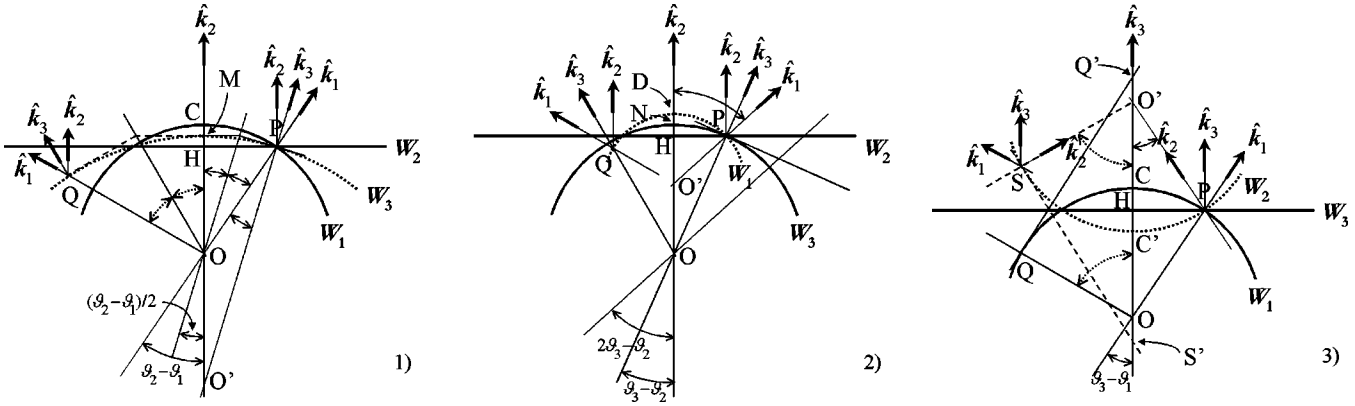

FIG. 2. Wave fronts $W_i (i=1,2,3)$ (dotted lines), generated by three-wave interactions in response to plane and spherical input wave fronts (full lines); $\hat{\mathbf{k}}_i$ are unit vectors parallel to the corresponding wave vectors. Panel (1): wave-front transformation in case 1 (see text). The input wave fronts W_1 and W_2 (object and reference, both at ω) cross at P and generate, at P, a SHG wave-front W_3 (hologram at 2ω) directed along the bisector of the angle $P\hat{O}H=\vartheta_2-\vartheta_1(P)$ and having eikonal $L_3(P)$ given by Eq. (22). The geometrical construction shows how to find the other points of the holographic wave front W_3. If the wave front transformed into W_3 is only a small region of the spherical wave front W_1, W_3 is virtually spherical with radius $2R$. Panel (2): wave-front transformation in case 2 (see text). The input wave fronts W_3 (object at 2ω) and W_2 (reference at ω) cross at P and generate, at P, a DFG wave front W_1 (hologram at ω) propagating at the angle $\vartheta_1=2\vartheta_3-\vartheta_2$. Within the same approximation as above, the wave front W_1 is spherical with radius $R/2$. Panel (3): wave-front transformation in case 3 (see text). The input wave front W_1 (object at ω) and W_3 (reference at 2ω) generate a DFG wave front W_2 (hologram at ω) propagating symmetrically to W_1 with respect to W_3. In this case the spherical wave front W_1 transforms into a perfectly spherical wave front W_2 with identical radius R. (See text for details.)

for any point Q of the object wave-front W_1 the distance HQ' represents the magnitude of the right-hand side in Eq. (25) and the corresponding point S of the DFG holographic wave front W_2 is located at the position shown in panel (3). In fact, the triangle $SS'O'$ is the mirror image of triangle $QQ'O$ with respect to the plane wave front W_3 and the distance HS' represents the first member of Eq. (25). In this case the spherical wave front W_1 emitted at O transforms into a perfectly spherical wave front W_2 with identical radius R converging to O'. The holographic image of any object is thus a one-to-one replica of the object. Moreover, the spatial resolution of the holographic image is rigorously identical to that of the object, of course if the image and object are observed through pupils of equal apertures. This is only approximately true in the two previous cases in which the reconstructed wave fronts (SHG W_3 in case 1 and DFG W_1 in case 2 are spherical only under restricting hypotheses). Note that in all cases the transverse dimensions of the holographic images are identical to those of the objects but only in the last case are the real/virtual nature, the longitudinal size and position (hence the whole shape), and the frequency all conserved on passing from the object to its holographic replica generated by the three-wave interaction.

II. EXPERIMENTS

We already checked the results in case 1 by performing experiments on real objects in the degenerate condition of second-harmonic generation, i.e., SHG holograms for which $\omega_1=\omega_2(=\omega)$ [5–8,24,25]. In this paper we present experiments in which holograms of pointlike sources of light are obtained by difference-frequency generation according to both cases 2 and 3 above. We still work at degeneracy and use either the fundamental or the frequency-doubled output of our pulsed laser as the reference field in the two cases. The frequency-doubled output of a Q-switched amplified neodymium-doped yttrium aluminum garnet (Nd:YAG) laser (model Quanta-Ray GCR-4, Spectra-Physics Inc., Mountain View, CA) was separated from the nonconverted output by a prism and both beams were suitably space filtered and shaped into collimated beams of about 2 mm diameter. Although a single beam at ω was necessary for either of the two cases of DFG, the infrared beam was split into two beams of similar intensity for aligning purposes. The polarizations were as in Fig. 1, the (y,z) plane being horizontal. The holograms obtained via DFG were produced in a nonlinear β-BaB_2O_4 (BBO) crystal, cut at 22.8° for 2ω generation at normal incidence in collinear PM I, with 5×5 mm^2 cross section and 2 mm thickness (Fujian Castech Crystals Inc., Fuzhou, China). Before each experiment the two beams at ω were aligned so as to cross at the crystal position by forming an angle of $\sim11°$ to each other and the BBO was angle-tuned to generate the noncollinear second harmonic beam. The output at 2ω from the laser was then superimposed on it until a down-converted beam was observed upon blanking one of the two beams at ω (slave beam at ω). In each experiment, the beam playing the role of the reference beam was enlarged by a telescope formed by two lenses of focal lengths -30 mm and $+100$ mm so as to widely illuminate the BBO crystal, whose cross section (slant for achieving noncollinear PM I, see Fig. 1) determined the effective pupil of our optical systems.

The setup for the experiment in case 2 is sketched in Fig. 3. The telescope was set on the beam at ω while the object O at 2ω was the focal spot of lens l_1 ($f_1=100$ mm). The charge-coupled device (CCD) camera to be used as the de-

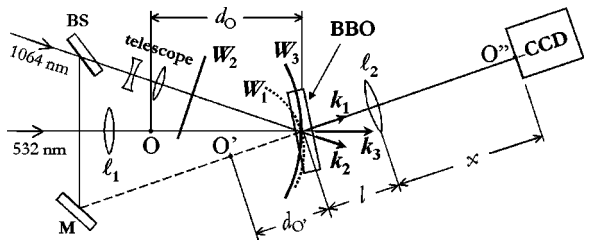

FIG. 3. Setup for the experiment of DFG in case 2. *M*: 100% reflectance mirror; BS: ~50% beam splitter; telescope: 3.3×; BBO: $\beta-BaB_2O_4$ crystal; CCD: camera; dashed beam: slave beam for prealigning the CCD. Lens l_1 ($f_1=100$ mm) forms the pointlike object source *O*. Lens l_2 ($f_2=150$ mm) forms the real image O'' of the virtual image O' created by the DFG wave front W_1.

tector (model PE2015, Pulnix Europe, Basingstoke, U.K.) was previously centered on the slave beam at ω. Since according to Eq. (15) the field generated by the BBO at ω reconstructs a virtual image O', a lens (l_2 in Fig. 3, $f_2=150$ mm) was inserted to obtain a real image on the CCD sensor.

Figure 4 shows the setup for the experiment in case 3 in which the reference beam, enlarged by the telescope, was the one at 2ω while the object *O* was the focal spot of lens l_1 ($f_1=100$ mm) set on the beam at ω. In this case, as expected from the result in Eq. (17), the image O' is real and hence directly detectable by the CCD.

In the experiment in case 2 the pointlike object *O* was formed by l_1 at a distance $d_O=29.5$ cm from the crystal BBO, and the distance between l_2 and BBO crystal was $l=16$ cm (see Fig. 3). The experiment was performed by using 2.8 mJ pulses in the green object beam and 38.6 mJ pulses in the ir reference beam. The image O'' formed by l_2 was detected on focus when the CCD was located at a distance $x=29.5$ cm from l_2. Figure 5 shows this image as an intensity map with full width at half maximum (FWHM) diameter of ~110 μm, in the vertical direction. By calculating the distance from the BBO crystal at which the holographic image O' is located ($d_{O'}$ in Fig. 3), we find $d_{O'}=1/(1/f_2-1/x)-l\cong 14.5$ cm, an experimental value that matches very well the value $d_O/2\cong 14.7$ cm expected from Eq. (26) and Fig. 2, panel (2). As to the shape of O' in the

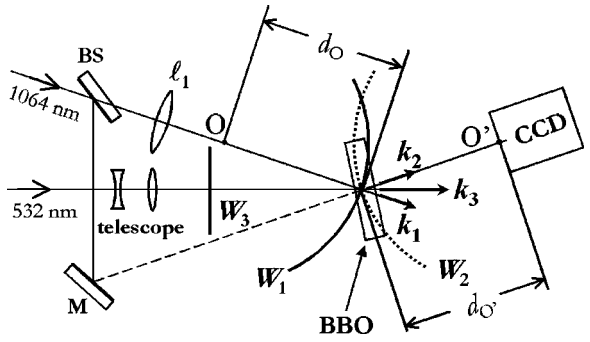

FIG. 4. Setup for the experiment of DFG in case 3. Lens l_1 ($f_1=100$ mm) forms the pointlike object source *O*. O' is the real image created by the DFG wave front W_2. Other symbols as in Fig. 3.

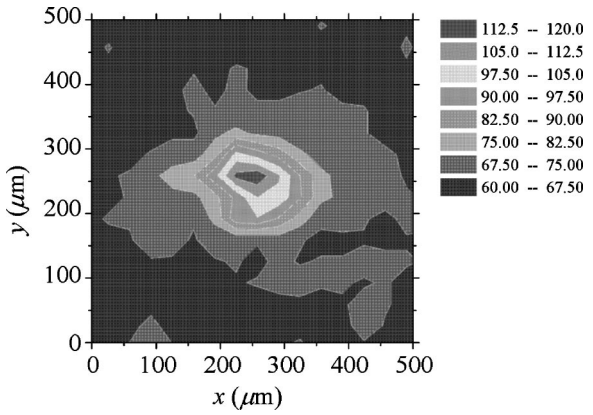

FIG. 5. Image O'' detected on focus by the CCD camera in case 2 (average of 50 repetitions).

transverse (x,y) plane, to be compared with that of *O*, we first note that it is equal to that of O'' in Fig. 5, due to the 1:1 magnification of the imaging through lens l_2. Moreover, *O* has a FWHM diameter of ~67 μm, which is the focal spot of a 2 mm diameter beam at 532 nm through l_1, and emits a wave front W_3 (see Fig. 3) fully covering the BBO cross section. For infinite cross section the holographic virtual image O' should also have FWHM diameter equal to ~67 μm since the down-converted wave front W_1 has double curvature and double wavelength as compared to W_3. Actually this is true only as long as the approximation of W_1 by a spherical wave front is acceptable.

As shown in Fig. 5 we find ~113 μm in the vertical direction. In the horizontal direction we find a little more, maybe because of the narrower aperture due to the tilt of the crystal that is necessary for achieving PM I among noncollinear wave vectors.

In the experiment in case 3 the pointlike object *O* was formed by l_1 at a distance $d_O=27$ cm from the crystal BBO, which within the experimental accuracy (<5 mm) was equal to the distance $d_{O'}$ (BBO crystal to CCD camera; see Fig. 4) at which the holographic image O' was detected in focus, in agreement with the result in panel (3) of Fig. 2. This experiment was performed by using 27.3 mJ pulses in the ir object beam and 1.8 mJ pulses in the green reference beam.

The detected real image O' is displayed in Fig. 6 as an intensity map. The FWHM diameter of the image is ~160 μm in the vertical direction and ~200 μm in the horizontal one. In this case, *O* being the focal spot of a 2 mm diameter beam at 1064 nm through l_1, its FWHM diameter is ~135 μm and the object wave front W_1 when it impinges on the crystal is almost as extended as was W_3 in the previous case. Again we find a DFG holographic spot image only slightly bigger than the object spot. The last experiment shows that the phase-conjugate version of any input wave front can be obtained, a result that remarkably strengthens the pioneering experimental work of Avizonis *et al.* [14].

CONCLUSIONS

We considered the parametric interaction in a $\chi^{(2)}$ nonlinear material (uniaxial crystal BBO) of three noncollinearly

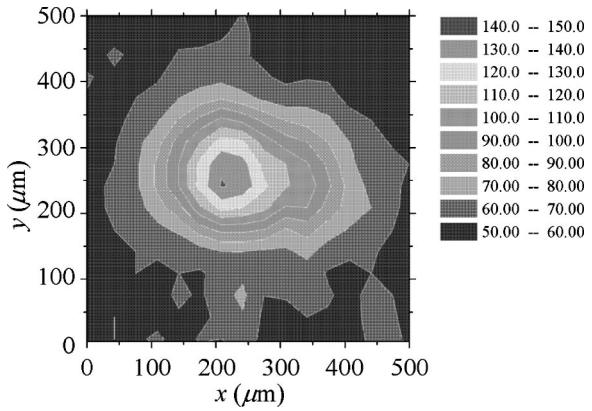

FIG. 6. Image O'' detected on focus by the CCD camera in case 3 (average of 50 repetitions).

propagating waves satisfying a type I phase-matching condition. We analytically solved the equations governing the interaction of fields at different frequencies for all initial conditions (three cases) of relevance to demonstrate that any sum or difference frequency interaction generates a field which is a holographic replica of the input field that plays the role of the object field. An analysis of the wave fronts performed through their eikonals allowed us to determine the position and shape of the image reconstructed by the generated wave front. The three cases, at degeneracy, were experimentally verified by adopting a pointlike source as the object. The distance of holographic image to crystal with respect to the distance of object to crystal scales exactly as expected from theory in each case. As to the transverse sizes of the holographic images, in the case of SHG holograms (case 1 in this paper) we already published a series of experiments demonstrating full agreement with the theory above [5–8,24,25]. Here, in two cases of DFG (with the object field at 2ω and reference at ω in case 2 and vice versa in case 3) we find agreement of the holographic spot sizes with the expected values. The agreement is better in the latter case, a result that also agrees with our theoretical treatment. In fact, case 3 is the only one in which the shape of the wave front reconstructed by the interaction is rigorously identical to that (spherical) of the object wave front [see Eq. (28) and panel (3) in Fig. 2]. The noticeable fact that this type of difference frequency generation in a phase-matched interaction occurring in noncollinear geometry provides exact phase-conjugated replicas of wave fronts with arbitrary shapes allows applications that go beyond those of real-time holography (e.g., see [25]). Moreover, the technique described in this paper can be applied, as it is, to phase conjugation of ultrashort pulses because we demonstrated its operation in BBO, a material in which group-velocity matching is achieved from blue to ir wavelengths via suitable noncollinear interaction geometries and the group-velocity dispersion is so negligible as to allow efficient conversion of pulses with tens of femtoseconds duration [9,10,26,27].

ACKNOWLEDGMENTS

We gratefully acknowledge the help of Yury N. Denisyuk, Ioffe Physico-Technical Institute, St. Petersburg, Russia, and the assistance of Marco Potenza and Emiliano Puddu. We also acknowledge fruitful discussions with Viktor N. Mikhailov, S. I. Vavilov State Optical Institute, St. Petersburg, Russia, during the revision phase of the manuscript.

APPENDIX

According to Eq. (1) the total field inside the crystal is

$$\boldsymbol{E}=\boldsymbol{E}_1+\boldsymbol{E}_2+\boldsymbol{E}_3=(E_1+E_2)\hat{\boldsymbol{x}}+E_{3y}\hat{\boldsymbol{y}}+E_{3z}\hat{\boldsymbol{z}} \tag{A1}$$

and satisfies the wave equation

$$\nabla^2\boldsymbol{E}-\frac{1}{c^2}\frac{\partial^2\boldsymbol{E}}{\partial t^2}=\mu_0\frac{\partial^2\boldsymbol{P}_{NL}}{\partial t^2}. \tag{A2}$$

It is convenient to consider a system of coordinates (X,Y,Z) intrinsic to the crystal, with Z along the optical axis and X parallel to x, because the calculation of the nonlinear polarization $\boldsymbol{P}_{NL}$ becomes straightforward:

$$\begin{pmatrix}(P_{NL})_X\\(P_{NL})_Y\\(P_{NL})_Z\end{pmatrix}=2\begin{pmatrix}0&0&0&0&d_{31}&-d_{22}\\-d_{22}&d_{22}&0&d_{31}&0&0\\d_{31}&d_{31}&d_{33}&0&0&0\end{pmatrix}\times\begin{pmatrix}E_X^2\\E_Y^2\\E_Z^2\\2E_YE_Z\\2E_XE_Z\\2E_XE_Y\end{pmatrix}, \tag{A3}$$

where the matrix contains the nonlinear coupling coefficients [28]. According to Fig. 1, we have

$$\begin{aligned}E_X&=\boldsymbol{E}\cdot\hat{\boldsymbol{X}}=E_1+E_2,\\E_Y&=\boldsymbol{E}\cdot\hat{\boldsymbol{Y}}=E_{3y}\hat{\boldsymbol{y}}\cdot\hat{\boldsymbol{Y}}+E_{3z}\hat{\boldsymbol{z}}\cdot\hat{\boldsymbol{Y}}\\&=E_{3y}\cos(\alpha-\vartheta_3)+E_{3z}\sin(\alpha-\vartheta_3),\\E_Z&=\boldsymbol{E}\cdot\hat{\boldsymbol{Z}}=E_{3y}\hat{\boldsymbol{y}}\cdot\hat{\boldsymbol{Z}}+E_{3z}\hat{\boldsymbol{z}}\cdot\hat{\boldsymbol{Z}}\\&=-E_{3y}\sin(\alpha-\vartheta_3)+E_{3z}\cos(\alpha-\vartheta_3).\end{aligned} \tag{A4}$$

Once the components of nonlinear polarization in the reference frame (X,Y,Z) are obtained, the direct substitution of Eq. (A4) into Eq. (A3) gives the components in the laboratory frame (x,y,z):

$$\begin{aligned}\boldsymbol{P}_{NL}\cdot\hat{\boldsymbol{x}}&=(P_{NL})_X\hat{\boldsymbol{X}}\cdot\hat{\boldsymbol{x}}=(P_{NL})_X,\\\boldsymbol{P}_{NL}\cdot\hat{\boldsymbol{y}}&=(P_{NL})_Y\hat{\boldsymbol{Y}}\cdot\hat{\boldsymbol{y}}+(P_{NL})_Z\hat{\boldsymbol{Z}}\cdot\hat{\boldsymbol{y}}\\&=(P_{NL})_Y\cos(\alpha-\vartheta_3)-(P_{NL})_Z\sin(\alpha-\vartheta_3),\end{aligned}$$

$$\boldsymbol{P}_{NL}\cdot\hat{\boldsymbol{z}}=(P_{NL})_Y\hat{\boldsymbol{Y}}\cdot\hat{\boldsymbol{z}}+(P_{NL})_Z\hat{\boldsymbol{Z}}\cdot\hat{\boldsymbol{z}}$$
$$=(P_{NL})_Y\sin(\alpha-\vartheta_3)+(P_{NL})_Z\cos(\alpha-\vartheta_3). \tag{A5}$$

We now consider the components of Eq. (A2) in the frame (x,y,z) and obtain the following system of equations:

$$\nabla^2(E_1+E_2)-\frac{1}{c^2}\frac{\partial^2(E_1+E_2)}{\partial t^2}=\mu_0\frac{\partial^2\boldsymbol{P}_{NL}\cdot\hat{\boldsymbol{x}}}{\partial t^2},$$
$$\nabla^2E_{3y}-\frac{1}{c^2}\frac{\partial^2E_{3y}}{\partial t^2}=\mu_0\frac{\partial^2\boldsymbol{P}_{NL}\cdot\hat{\boldsymbol{y}}}{\partial t^2},$$
$$\nabla^2E_{3z}-\frac{1}{c^2}\frac{\partial^2E_{3z}}{\partial t^2}=\mu_0\frac{\partial^2\boldsymbol{P}_{NL}\cdot\hat{\boldsymbol{z}}}{\partial t^2}. \tag{A6}$$

The second members of these equations contain a number of terms at different frequencies, while each term in the first members depends on only one of the frequencies $\omega_1,\omega_2,\omega_3$. Thus by equating the terms at the same frequency we get

$$\nabla^2E_1-\frac{1}{c^2}\frac{\partial^2E_1}{\partial t^2}=4\omega_1^2[d_+E_{3y}+d_-E_{3z}]E_2^*,$$
$$\nabla^2E_2-\frac{1}{c^2}\frac{\partial^2E_2}{\partial t^2}=4\omega_2^2[d_+E_{3y}+d_-E_{3z}]E_1^*,$$
$$\nabla^2E_{3y}-\frac{1}{c^2}\frac{\partial^2E_{3y}}{\partial t^2}=4\omega_3^2d_+E_1E_2,$$
$$\nabla^2E_{3z}-\frac{1}{c^2}\frac{\partial^2E_{3z}}{\partial t^2}=4\omega_3^2d_-E_1E_2, \tag{A7}$$

where we have defined

$$d_+=d_{22}\cos(\alpha-\vartheta_3)+d_{31}\sin(\alpha-\vartheta_3),$$
$$d_-=d_{22}\sin(\alpha-\vartheta_3)-d_{31}\cos(\alpha-\vartheta_3). \tag{A8}$$

We now proceed to evaluate the first members of Eq. (A7) for the fields in Eq. (1):

$$\nabla^2E_1-\frac{1}{c^2}\frac{\partial^2E_1}{\partial t^2}=\frac{1}{2}\sqrt{\frac{2\eta_0\hbar\omega_1}{n_1}}\exp[-i(k_1\cos\vartheta_1z+k_1\sin\vartheta_1y-\omega_1t)]\left\{\frac{\partial^2a_1(\boldsymbol{r})}{\partial y^2}-2ik_1\sin\vartheta_1\frac{\partial a_1(\boldsymbol{r})}{\partial y}-k_1^2\sin^2\vartheta_1a_1(\boldsymbol{r})+\frac{\partial^2a_1(\boldsymbol{r})}{\partial z^2}-2ik_1\cos\vartheta_1\frac{\partial a_1(\boldsymbol{r})}{\partial z}-k_1^2\cos^2\vartheta_1a_1(\boldsymbol{r})+k_1^2a_1(\boldsymbol{r})\right\}+\text{c.c.}$$
$$=\frac{1}{2}\sqrt{\frac{2\eta_0\hbar\omega_1}{n_1}}\exp[-i(k_1\cos\vartheta_1z+k_1\sin\vartheta_1y-\omega_1t)]\left\{-2ik_1\sin\vartheta_1\times\frac{\partial a_1(\boldsymbol{r})}{\partial y}-2ik_1\cos\vartheta_1\frac{\partial a_1(\boldsymbol{r})}{\partial z}\right\}+\text{c.c.}, \tag{A9}$$

where we choose to neglect the second derivatives. By repeating the same procedure for the other fields, we obtain the system in Eq. (2). We checked *a posteriori* that the analytical solutions $a_j(\boldsymbol{r})$ to system (2) allow such a ''slowly varying envelope'' approximation in all cases.

[1] A.X. Shen, A.D. Nguyen, J.W. Perry, D.L. Huestis, and R. Kachru, Science **278**, 96 (1997).
[2] O. Matoba, K. Itoh, and K. Kuroda, Proc. IEEE **87**, 2030 (1999).
[3] P.C. Sun and K. Oba, Proc. IEEE **87**, 2086 (1999).
[4] J.A. Ma, T. Chang, S. Choi, and J. Hong, Opt. Quantum Electron. **32**, 383 (2000).
[5] Y.N. Denisyuk, A. Andreoni, and M.A.C. Potenza, Opt. Mem. Neural Networks **8**, 123 (1999).
[6] A. Andreoni, M. Bondani, Y.N. Denisyuk, and M.A.C. Potenza, J. Opt. Soc. Am. B **17**, 977 (2000).
[7] Y.N. Denisyuk, A. Andreoni, M. Bondani, and M.A.C. Potenza, Opt. Lett. **25**, 890 (2000).
[8] Y.N. Denisyuk, A. Andreoni, M. Bondani, and M.A.C. Potenza, Opt. Spectrosc. **89**, 113 (2000).
[9] A. Andreoni, M. Bondani, and M.A.C. Potenza, Opt. Commun. **154**, 376 (1998).
[10] A. Andreoni and M. Bondani, Appl. Opt. **37**, 2414 (1998).
[11] A. Andreoni, M. Bondani, M.A.C. Potenza, and F. Villani, J. Nonlinear Opt. Phys. Mater. **8**, 55 (1999).
[12] A. Andreoni, M. Bondani, M.A.C. Potenza, and F. Villani, Eur. Phys. J. D **8**, 111 (2000).
[13] A. Andreoni and M. Bondani, Opt. Commun. **174**, 487 (2000).
[14] P.V. Avizonis, F.A. Hopf, W.D. Bomberger, S.F. Jacobs, A. Tomita, and K.H. Womack, Appl. Phys. Lett. **31**, 435 (1977).
[15] S.N. Shostko, Y.G. Podoba, Y.A. Ananiev, B.D. Volosov, and A.M. Gorlanov, Pis'ma Zh. Eksp. Teor. Fiz. **5**, 29 (1979).
[16] A.M. Gorlanov, N.I. Grishmanova, N.A. Sventsitskaya, and V.D. Solov'yov, Kvant. Elektron. (Moscow) **5**, 415 (1982).
[17] D.M. Pepper and A. Yariv, in *Optical Phase Conjugation*, edited by R. Fisher (Academic Press, New York, 1983), p. 23.
[18] B. Zel'dovich, *Wave Front Conjugation* (Science, Moscow, 1985).

[19] L. Lefort and A. Barthelemy, Opt. Lett. **21**, 848 (1996).
[20] M.R. Fewings and A.L. Gaeta, J. Opt. Soc. Am. B **17**, 1522 (2000).
[21] P.D. Trapani, W. Chinaglia, G. Valiulis, and A. Andreoni, Phys. Rev. Lett. **80**, 265 (1998).
[22] D. Gabor, Proc. R. Soc. London, Ser. A **197**, 454 (1949).
[23] J. W. Goodman, *Introduction to Fourier Optics* (McGraw-Hill, New York, 1988).
[24] A. Andreoni, M. Bondani, and M.A.C. Potenza, Opt. Lett. **25**, 1570 (2000).
[25] A. Andreoni, M. Bondani, Y.N. Denisyuk, M.A.C. Potenza, and E. Puddu, Rev. Sci. Instrum. **72**, 2525 (2001).
[26] P.D. Trapani, A. Andreoni, G.P. Banfi, C. Solcia, R. Danielius, A. Piskarskas, P. Foggi, M. Monguzzi, and C. Sozzi, Phys. Rev. A **51**, 3164 (1995).
[27] P.D. Trapani, A. Andreoni, C. Solcia, P. Foggi, R. Danielius, A. Dubietis, and A. Piskarskas, J. Opt. Soc. Am. B **12**, 2237 (1995).
[28] V.G. Dmitriev, G.G. Gurzadyan, and D.N. Nikogosyan, *Handbook of Nonlinear Optical Crystals* (Springer, Berlin, 1997).